sustainability

MDPI

Article

A 3D BEM Model for the Hydrodynamic Analysis and Design of Heaving WEC Arrays Attached to a Breakwater

Alexandros Magkouris [1], Markos Bonovas [1], Theodoros Gerostathis [2] and Kostas Belibassakis [1,*]

[1] School of Naval Architecture & Marine Engineering, National Technical University of Athens (NTUA), 15780 Athens, Greece; alexmagouris@mail.ntua.gr (A.M.); markosbonovas@hotmail.gr (M.B.)
[2] Department of Naval Architecture, School of Engineering, University of Western Attica, 12243 Athens, Greece; tgero@uniwa.gr
* Correspondence: kbel@fluid.mech.ntua.gr

Abstract: Assessment of the performance of arrays of wave energy converters (WECs) of the type of simple heaving floaters, operating in nearshore and coastal areas, is essential to estimate their power production capacity. The effective design and layout of such WEC farms can be supported by studying the system's operational characteristics based on the wave climatology of the deployment region. Installation along the exposed side of harbor breakwaters in sea areas with substantial incoming energy potential is a promising option. In this study, a 3D hydrodynamic model based on the boundary element method (BEM) is presented and discussed, aiming to evaluate the performance of WEC arrays consisting of multiple heaving bodies attached to the exposed side of a harbor breakwater, modelled as a vertical wall, considering its reflective effects, as well as hydrodynamic interactions between the multiple floating devices. Numerical results of the predicted power performance for various configurations, including interactions of multiple WECs with the nearshore topography and the breakwater wall, as well as the effects of power take off (PTO) parameters, are presented and discussed. Finally, a case study is presented for a selected coastal site at the port of Heraklion, located in the north-central part of Crete Island in the South Aegean Sea, characterized by relatively increased wave energy potential, using long-term climatological data, illustrating the method and its applicability as a supporting tool for optimal design of WEC arrangements.

Keywords: wave energy; WEC arrangements; breakwater installation; 3D BEM; hydrodynamic analysis

Citation: Magkouris, A.; Bonovas, M.; Gerostathis, T.; Belibassakis, K. A 3D BEM Model for the Hydrodynamic Analysis and Design of Heaving WEC Arrays Attached to a Breakwater. *Sustainability* **2023**, *15*, 12777. https://doi.org/10.3390/su151712777

Academic Editor: Ching-Piao Tsai

Received: 29 July 2023
Revised: 17 August 2023
Accepted: 22 August 2023
Published: 23 August 2023

1. Introduction

Marine renewable sources are currently actively contributing to energy decarbonization and the development of sustainable energy policies. Wave energy converters (WECs) of the type of simple heaving point absorbers, installed in nearshore and coastal areas, constitute one of the most widespread systems in wave energy harnessing; see, e.g., [1]. In this regard, the performance assessment of WECs is essential for determining structural and functional features, evaluating wave power absorption, as well as for the optimum layout and design of WEC farms. Coastal areas, in general, are characterized by shallow and often varying seabed topography, which can affect optimal design and alter the achieved power performance. In Ref. [2], this effect is quantified by using appropriate tools. The methodology can be used for basic research and design of WEC farms due to the low computational cost required; see also [3–5]. Moreover, a simplified model based on the modified mild-slope equation, capable of simulating wave scattering by arrays of simple heaving point absorbers in general bottom topography, is presented in Ref. [6]. The possibility of installing WEC arrays on the exposed side of breakwaters or piers was a subject of research in the past few years; see Figure 1. Apart from obvious benefits regarding the facilitation of installation and maintenance, this can also augment the captured wave

energy, due to effects of wall reflections that increase the responses; see, e.g., [7,8]. Recently, such deployments were tested in areas of increased wave potential, as in the case of the breakwater in the port of Heraklion in the northern-central part of Crete Island by SINN Power (https://www.sinnpower.com, accessed on 29 July 2023), as shown in Figure 1b. In such cases, the evaluation of long-term performance is supported by using high-quality, many years-long time series of wave data; see also [9]. In addition, WEC-type absorbers integrated into floating breakwaters were both numerically and experimentally studied by Cheng et al. [10], and the effects of various parameters and wave non-linearity are discussed. Additionally, integrated systems of breakwater WECs with other renewable energy converters for applications in the marine environment were recently studied and improvements of the combined performance are reported; see, e.g., [11,12].

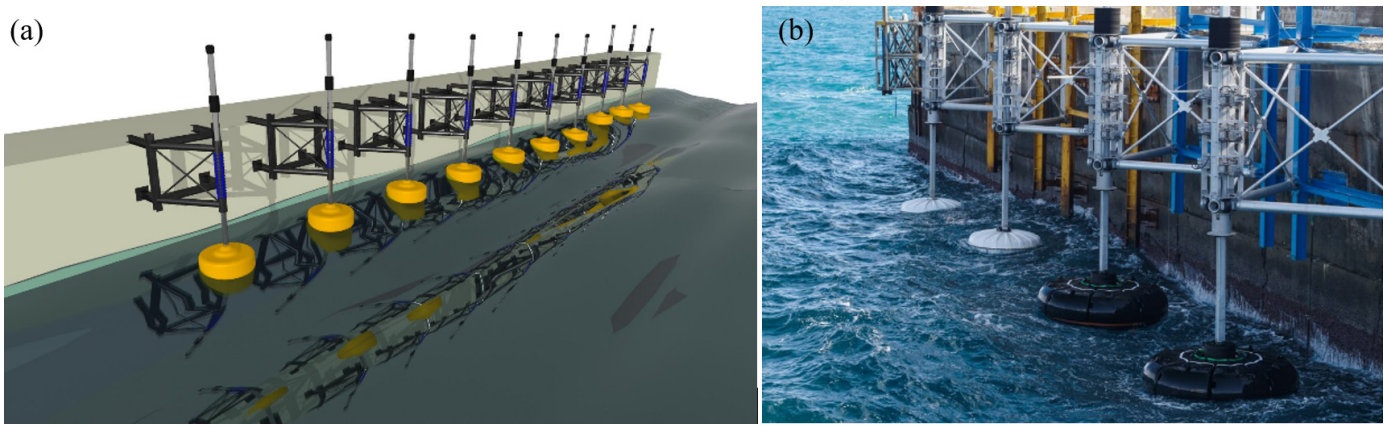

Figure 1. (**a**) Array of heaving-type wave energy converters (WECs) attached to a vertical wall. (**b**) Installation of WECs at the breakwater of the port of Heraklion, Crete Island, Greece by SINN power.

Moreover, existing studies show that, for the hydrodynamic problems of multiple floating bodies, the so-called "gap resonance" phenomenon occurs in the narrow gap between the floating bodies when they are placed in close proximity [13]. The occurrence of gap resonance could be helpful for improving the wave energy conversion efficiency of WECs. It was shown that when the gap resonance phenomenon occurs, the influence of fluid viscosity becomes significant, particularly for the heave motion of the floating structures [14,15], and should be considered; see also [16,17]. Although the classical potential flow theory does not consider the influence of fluid viscosity, which could lead to significant deviations at specific frequencies, it still provides useful results in an extended frequency band, which could be exploited for the evaluation of the system performance based on spectral average characteristics of the array response.

In this work, a 3D hydrodynamic model based on the boundary element method (3D BEM) is presented and discussed, aiming to evaluate the performance of WEC arrays consisting of multiple heaving bodies attached to the exposed side of a port breakwater. The latter is modelled as a vertical wall, taking into consideration reflective effects by the breakwater as well as hydrodynamic interactions between the multiple floating devices. Specifically, reflection effects are included in the BEM solver, assuming the deployment of a device at the exposed side of a breakwater. Numerical results of the predictions of power performance for various configurations are derived and discussed, including interactions of multiple WECs with the nearshore topography and the breakwater wall, as well as the effects of power take off (PTO) parameters. An important contribution of the present work is the development and testing of a first-order model that could provide, with relatively low cost, useful data for the preliminary design of complex WEC arrangements on breakwaters, over an extended incident wave frequency direction band, considering the long-term wave climatology of the installation site. The results could essentially support

the selection of basic parameters including the PTO system and the preliminary evaluation of capital expenditures and operating expenses. As a demonstrative example, a case study is presented for a selected coastal site at the port of Heraklion, located in the north-central part of Crete Island in the South Aegean Sea, characterized by relatively increased wave energy potential in the region. Using long-term climatological data, the present method is illustrated and its applicability as a supporting tool for optimal design purposes is discussed.

The present work investigates the 3D hydrodynamic problem of several interacting heaving WECs, forming an array attached to a breakwater, based on linear wave theory. The method can be extended to investigate more general shapes of axisymmetric floaters in one or more degrees of freedom, as well as to study the effects of various control strategies, such as latching techniques to maximize the power output of the devices, by constraining some of the operational characteristics. The structure of the present paper is as follows: In Section 2 the mathematical formulation of diffraction and radiation problems, involving multiple interactions of floating bodies operating as WEC point absorbers in front of a vertical wall, is presented, and the developed 3D boundary element method is discussed. Verification of the present model is included in Section 3, along with discussion concerning numerical convergence. Systematic results for selected configurations are presented in Section 4, also including the performance index of various members of the array. In Section 5, the long-term performance analysis in the case of a particular site is examined using long-term climatological data. Annual and seasonal statistics of the power output prediction by the system are presented and discussed. Finally, in the last section (Section 6), conclusive remarks are provided and directions for future research are discussed.

2. Mathematical Formulation and 3D BEM

We consider an array of (single DoF) heaving point absorber WECs, consisting of M identical devices, attached to the exposed side of a breakwater, and operating in constant local depth h as shown in Figure 2. The devices are subjected to harmonic wave excitation. The magnitude and phase of each WEC's heave oscillation is derived by the analysis of the surrounding flow field in the domain D, taking into account the hydrodynamic interactions among the WECs, as well as reflection effects due to the breakwater; see Figure 3. Based on standard floating body hydrodynamic theory, the total field is decomposed into the incident, the diffracted and M radiated subfields. The velocity field of each of the above is represented by the gradient of the corresponding potential function $\Phi_0(\mathbf{x};t)$, $\Phi_d(\mathbf{x};t)$, and $\Phi_m(\mathbf{x};t)$, $m = 1, 2, \ldots, M$.

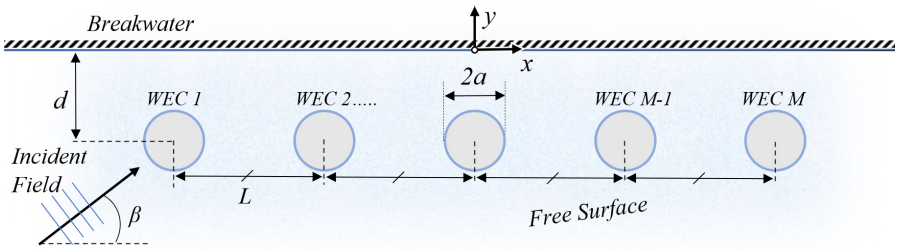

Figure 2. Top view of the considered configuration, illustrating basic dimensions.

The coordinate system $\mathbf{x} = (x, y, z)$ is used, with the origin placed at mean water level (MWL) at the position of the vertical wall so that the center of each WEC's waterplane area is located on the line $y = -d$, parallel to the breakwater. The origin is selected so that the whole configuration is symmetric with respect to the yz-plane, as schematically shown in Figures 2 and 3. In this work's context, cylindrical-shaped WECs of radius a and draft T are considered. However, the methodology presented can easily be extended to any device geometry. Results concerning the effect of different WEC shapes will be investigated in future works.

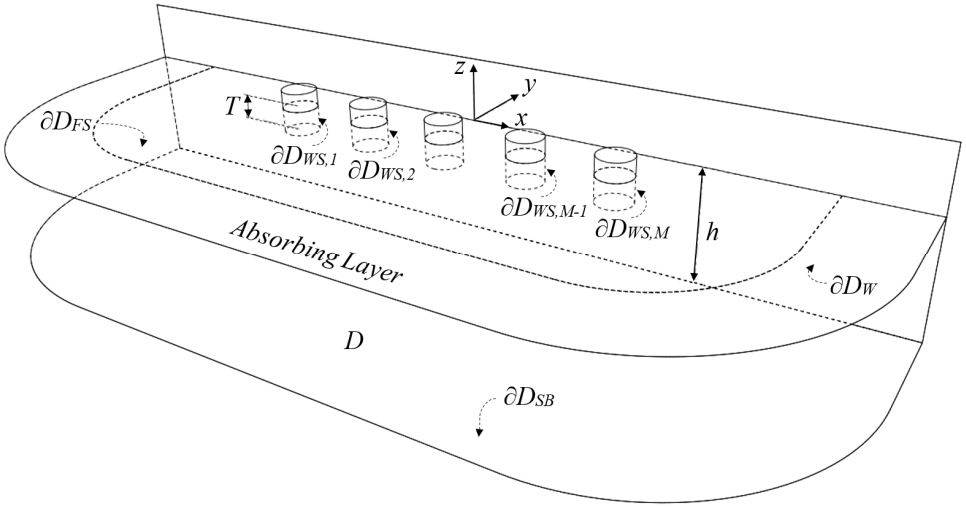

Figure 3. 3D sketch of the configuration, illustrating the various parts of the flow field boundary.

The above interaction problem is treated in the frequency domain, assuming harmonic time dependence in the form $\exp(-i\omega t)$, with ω being the angular frequency and $i = \sqrt{-1}$ the imaginary unit, by the representation:

$$\Phi(\mathbf{x};t) = \Phi_0(\mathbf{x};t) + \Phi_d(\mathbf{x};t) + \sum_{m=1}^{M} \frac{d\xi_m}{dt}\Phi_m(\mathbf{x};t) = \mathrm{Re}\left\{-\frac{igA}{\omega}\varphi(\mathbf{x})\cdot\exp(-i\omega\, t)\right\} \quad (1)$$

where A is the incident wave amplitude, g is the acceleration due to gravity, ξ_m denotes the complex amplitude of the *mth* WEC's oscillation in the z-direction, and $\varphi(\mathbf{x})$ is the complex potential in the frequency domain, which is given by:

$$\varphi(\mathbf{x}) = -i\omega\left\{\varphi_0(\mathbf{x}) + \varphi_d(\mathbf{x}) + \sum_{m=1}^{M}\xi_m\,\varphi_m(\mathbf{x})\right\}. \quad (2)$$

In Equation (2), $-i\omega\varphi_0$ and $-i\omega\varphi_d$ stand for the complex amplitudes of the incident and the diffracted subfields, respectively, and $\varphi_m,\ m = 1, 2, \ldots, M$ denote the complex amplitudes of $\Phi_m(\mathbf{x};t),\ m = 1, 2, \ldots, M$, evaluated for $\xi_m = 1$. The complex potential of the incident field, incorporating the reflection effects due to the presence of the vertical wall, is assumed to be known, and for unit wave amplitude $A = 1$ is given by:

$$\varphi_0(\mathbf{x}) = \frac{g}{\omega^2}\frac{\cosh(k[z+h])}{\cosh(kh)}F(x,y,\beta), \quad (3a)$$

where

$$F(x,y,\beta) = \exp(ik(\cos(\beta)x + \sin(\beta)y)) + R\exp(ik(\cos(-\beta)x + \sin(-\beta)y)). \quad (3b)$$

In the above equations, β is the propagation direction (also shown in Figure 2) and R is the reflection coefficient, which eliminates the reflection of the incident field (R = 0) in case of propagation parallel to the wall ($\beta = 0°$ or $\beta = 180°$) or generates the reflected field (R = 1) otherwise. Furthermore, k stands for the wavenumber, obtained by the dispersion relation, as formulated in the local depth h:

$$\omega^2 = k\,g\tanh(kh). \quad (4)$$

It is noted that Equation (3) presupposes a fully reflective vertical boundary of infinite length. The limitations of this assumption are investigated in Ref. [7], where it is shown

that it leads to reduced accuracy as regards the estimation of the heave excitation forces, especially at low frequencies, compared to more realistic, finite-length breakwater cases.

The diffraction and the M radiation subfields are evaluated by boundary value problems (BVPs), governed by the Laplace equation, and supplemented by appropriate boundary conditions (BCs) at the various parts of the boundary ∂D of the flow domain. The latter consists of the free surface of the water (∂D_{FS}), the wetted surfaces of the WECs ($\partial D_{WS,m}$, m = 1,2,. . .,M), the impermeable boundaries of the wall (∂D_W), and the seabed (∂D_{SB}); see also Figure 3. Impermeability BCs apply to the solid boundaries, while the linearized free surface boundary condition (FSBC) applies to ∂D_{FS}. Therefore, the diffracted and radiated fields are evaluated as solutions to the following BVPs:

$$\nabla^2 \varphi_m(\mathbf{x}) = 0, \ \mathbf{x} \in D, \ \ m = d, 1, 2, \ldots, M \tag{5a}$$

$$\frac{\partial \varphi_m(\mathbf{x})}{\partial n} - \mu\,(\mathbf{x};\ \omega)\varphi_m(\mathbf{x}) = 0, \quad \mathbf{x} \in \partial D_{FS}, \ \ m = d, 1, 2, \ldots, M, \tag{5b}$$

$$\frac{\partial \varphi_d(\mathbf{x})}{\partial n} = -\frac{\partial \varphi_0(\mathbf{x})}{\partial n}, \quad \mathbf{x} \in \bigcup_{m=1}^{M} \partial D_{WS,m}, \tag{5c}$$

$$\frac{\partial \varphi_m(\mathbf{x})}{\partial n} = \delta_{m\ell}\, n_3^{\ell}(\mathbf{x}), \ \ \mathbf{x} \in \partial D_{WS,\ell}, \ \ m, \ell = 1, 2, \ldots, M\ , \tag{5d}$$

$$\frac{\partial \varphi_m(\mathbf{x})}{\partial n} = 0, \ \ \mathbf{x} \in \partial D_{SB} \cup \partial D_W, \ m = d, 1, 2, \ldots, M\ , \tag{5e}$$

where $\mathbf{n} = (n_1, n_2, n_3)$ is the unit vector normal to ∂D, directed toward the exterior of the flow domain, and $\delta_{m\ell}$ in Equation (5d) is the Kronecker delta. The latter equation translates to the fact that the evaluation of the *m-th* radiation field is achieved by enforcing unit excitation of the *m-th* wetted surface, while treating the rest of the WECs as immobile and impermeable. Moreover, $\mu = \omega^2/g$ is the frequency parameter, which is expressed as a function of space in Equation (5b) to account for modifications analyzed hereafter. The wave solutions calculated by the above BVPs propagate undisturbed towards infinity, which suggests that the flow domain extents infinitely to all azimuthal directions $\theta = tan^{-1}(y, x) \in [\pi, 2\pi]$. Therefore, numerical treatment requires the above problems to be supplemented by appropriate conditions at infinity. Truncation of the flow domain is achieved by adopting a perfectly matched layer (PML) technique (see Figure 3), consisting of an absorbing layer, which is used to attenuate outgoing wave solutions and treat the radiating behaviour of the calculated fields at far distances from the WEC array, as described in detail in Ref. [2]. The damping of outgoing waves with minimal reflection depends on the thickness of the layer, which is taken to be of the order of one wavelength $\lambda = 2\pi/k$, while its coefficient is taken to be increasing within the layer. Implementation of the PML technique is achieved by making the frequency parameter complex within the layer to approximate artificial weakening of the wave solutions. Specifically, the frequency parameter is redefined as follows:

$$\mu(\mathbf{x};\ \omega) = \begin{cases} \omega^2 g^{-1}, & |\mathbf{x}| < R_{PML}[\theta(\mathbf{x})] \\ \omega^2 g^{-1}\left(1 + ic\frac{(|\mathbf{x}| - R_{PML}[\theta(\mathbf{x})])^{\,n}}{\lambda^n}\right)^2, & |\mathbf{x}| \geq R_{PML}[\theta(\mathbf{x})] \end{cases}, \tag{6}$$

where $R_{PML}\ [\theta(\mathbf{x})]$ denotes the PML activation radius in the direction $\theta(\mathbf{x}) = tan^{-1}(y/x)$. The PML is activated on a curve defined on the MWL plane, as shown in Figure 3. The parameter c and the exponent n are used as optimized in previous works [2], aiming to the maximization of the layer's efficiency, preventing numerical reflections, and avoiding contamination of the evaluated fields.

The BVPs described by Equation (5) are treated by means of a low-order panel method, based on simple singularity distributions and 4-node quadrilateral boundary elements,

ensuring continuity of the geometry of the various parts of the boundary [2]. The complex potential functions $\varphi_m, m = d, 1, 2, \ldots M$, are represented by:

$$\varphi_m(\mathbf{x}) = \int_{\widehat{\partial D}} \sigma_m(\mathbf{x}') \cdot \hat{G}(\mathbf{x}'|\mathbf{x}) dS(\mathbf{x}'), \quad \mathbf{x} \in D, \mathbf{x}' \in \widehat{\partial D}, \ m = d, 1, 2, \ldots M. \tag{7}$$

In Equation (7), $\partial\hat{D}$ denotes the boundary of D, excluding the seabed part (∂D_{SB}), while the homogeneous Neumann BC on the latter part is accounted for by using the following Green's function for the Laplace equation in 3D in Equation (7):

$$\hat{G}(\mathbf{x}'|\mathbf{x}) = G(\mathbf{x}'|\mathbf{x}) + G(\mathbf{x}'|\hat{\mathbf{x}}), \tag{8}$$

which involves the contribution by the mirror point $\hat{\mathbf{x}} = (x, y, -2h - z)$ with respect to the horizontal seabed plane $z = -h$. Furthermore, $\sigma_m(\mathbf{x}')$, $m = d, 1, 2, \ldots,$ and M are singularity strength distributions defined on the boundary $\partial\hat{D}$, which are obtained by means of the low-order panel method, under the assumption of being piecewise constant on each element. The above distributions, in conjunction with a discretized form of Equation (7), reproduce the fields φ_m, $m = d, 1, 2, \ldots, M$. Specifically, the potential functions and the corresponding velocity fields are approximated by:

$$\varphi(\mathbf{x}) = \sum_p \sigma_p \Phi_p(\mathbf{x}), \nabla\varphi(\mathbf{x}) = \sum_p \sigma_p \mathbf{U}_p(\mathbf{x}) \tag{9}$$

where the summation ranges over all panels, indexed by p, σ_p, is the singularity distribution's strength on the *p-th* element, while Φ_p and $\mathbf{U}_p$, respectively, denote induced potential and velocity from the *p-th* element (carrying unit singularity distribution), to the field point $\mathbf{x}$; for more details see [18].

The numerical solutions are obtained using a collocation technique, satisfying each BC at the centroid of the corresponding panels on the different parts of the boundary (i.e., wetted surfaces, free surface, and wall). The impermeability BC on $z = -h$ is universally satisfied due to contributions by the mirrored points, while the computational boundary mesh does not need to include ∂D_{SB}, significantly reducing the computational cost. Using constant normal dipole distributions on each quadrilateral element, the induced potential matrix is analytically calculated via the solid angle; see [19]. Moreover, exploiting the equivalence of a constant dipole element to a vortex ring, the calculation of induced velocity is obtained by repetitive use of the Biot–Savart law [18]. As concerns discretization, a minimum of 15–20 elements per wavelength is applied to the discretization of the free surface boundary to eliminate numerical errors due to the damping and dispersion associated with the above numerical scheme.

An important aspect of the BEM formulation is the mesh generation. The discretization is accomplished by incorporating corresponding structured meshes on the various boundary surfaces. Other important features are the continuous junctions between the different parts of the mesh, which, in conjunction with the quadrilateral elements, ensure global continuity of the boundary. An indicative boundary mesh of the flow domain consisting of 12,332 quadrilateral elements and containing 5 cylindrical WECs is presented in Figures 4 and 5. As shown in these figures, sections of the free surface mesh are defined around each WEC to achieve continuity of the discretization. The surrounding free surface mesh spans a certain number of wavelengths and incorporates the absorbing layer. Furthermore, increased grid resolution is applied to the near field and on the wetted surfaces of the WECs for obtaining better quality results.

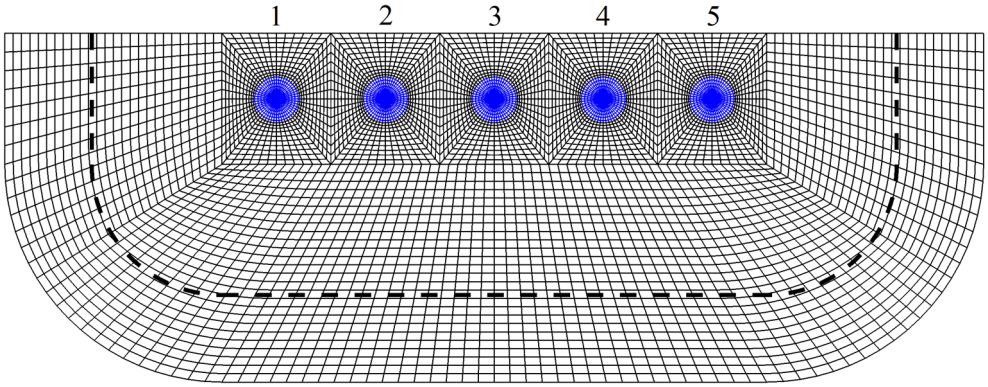

Figure 4. Top view of boundary mesh with the PML activation curve marked by a thick dashed line. The numbering of WECs is also indicated.

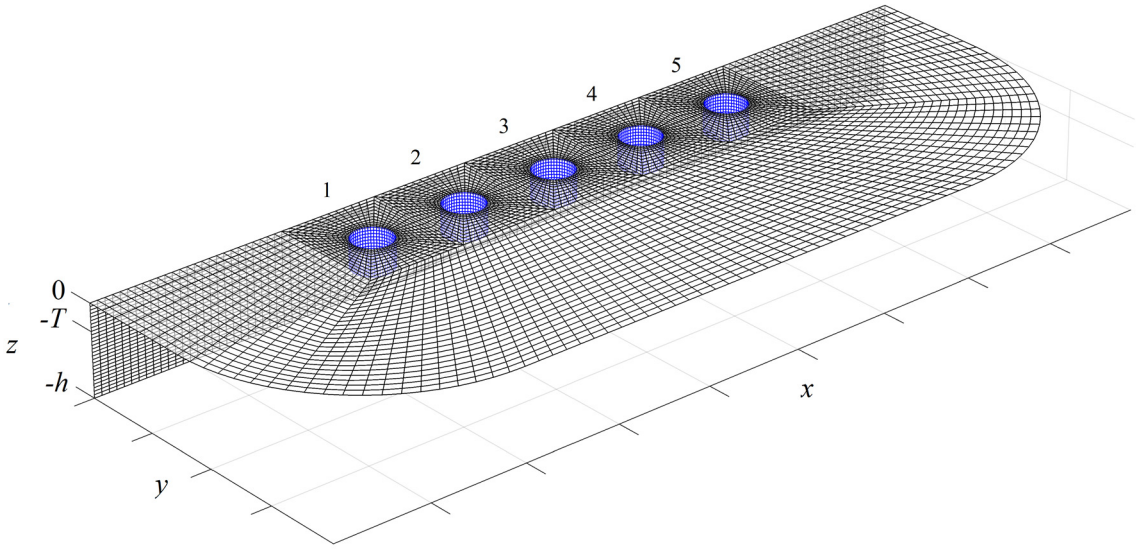

Figure 5. 3D view of arrangement and boundary mesh, also indicating the numbering of the WECs.

Having calculated the diffracted and radiated subfields, the heave response ξ_m, $m = 1, 2, \ldots, M$ of each WEC in the array is obtained by the following $M \times M$ linear system:

$$\left[-\omega^2(\mathbf{M} + \mathbf{A}(\omega)) - i\omega(\mathbf{B}(\omega) + \mathbf{B}_{PTO}) + (\mathbf{C} + \mathbf{C}_{PTO})\right]\boldsymbol{\xi} = \mathbf{F} = \mathbf{F}_0 + \mathbf{F}_d. \quad (10)$$

In Equation (10), the inertia of the WECs is modelled by the diagonal matrix $\mathbf{M} = M\mathbf{I}$, with $M = \rho\pi a^2 T$, where ρ is the water density. Furthermore, the effect of the hydrostatic restoring forces is modelled by the diagonal matrix $\mathbf{C} = c_{33}\mathbf{I}$, where $\mathbf{I}$ is the identity matrix, and $c_{33} = \rho g \pi a^2$ is the heave hydrostatic coefficient, with a being the WEC radius. In addition, $\mathbf{B}_{PTO} = B_{PTO}\mathbf{I}$ models the extraction of energy from the power take off system, which is achieved by an additional damping coefficient, and $\mathbf{C}_{PTO} = C_{PTO}\mathbf{I}$ is the PTO stiffness. The elements of the added mass and hydrodynamic damping matrices $\mathbf{A}(\omega)$ and $\mathbf{B}(\omega)$, respectively, are obtained via the calculated radiation fields as:

$$\omega^2 A_{m\ell} + i\omega B_{m\ell} = \rho \int_{\partial D_{WS,m}} \varphi_\ell(\mathbf{x}) \cdot n_3(\mathbf{x}) dS(\mathbf{x}),\ \mathbf{x} \in \partial D_{WS,m},\ \ m, \ell = 1, 2, \ldots, M \quad (11)$$

Moreover, the Froude–Krylov and the diffraction excitation forces on the *m-th* WEC are calculated by integration of the pressure induced by each of the fields multiplied by the vertical component of the normal vector **n**:

$$F_{\ell,m} = \omega^2 \rho \int\limits_{\partial D_{WS,m}} \varphi_\ell(\mathbf{x}) \cdot n_3(\mathbf{x}) dS(\mathbf{x}),\ x \in \partial D_{WS,m},\ \ell = 0, d,\ m = 1, 2, \ldots, M \quad (12)$$

The mean output power of the each WEC device is then evaluated as:

$$P_{OUT,m} = \frac{1}{2} \eta_{eff}\, \omega^2 B_{PTO} |\xi_m|^2, \quad (13)$$

where η_{eff} stands for the efficiency of the electromechanical PTO system, and thus the performance index is defined by normalizing the above result with respect to the incident wave power flux over the cross section of the device, given by the WEC waterline diameter, considering a wave of height $H = 2A$:

$$P_m = \frac{P_{OUT,m}}{0.25 \rho g H^2 C_g a} \quad (14)$$

where C_g denotes the wave group velocity.

3. Model Verification

In this section, results obtained by the present model are compared against data from previous research for verification. The total Froude–Krylov (FK) and diffraction vertical forces exerted on five cylindrical WECs of an array operating in a region of water depth $h = 10$ m in front of a vertical impermeable wall are examined; see Figure 5. The propagation direction is $\beta = 90^\circ$, corresponding to normal wave incidence to the wall, and thus, both the incident and diffracted fields present symmetry with respect to the central body. Therefore, the total forces acting on the devices 1 and 5, as well as the ones acting on devices 2 and 4, are the same. The WECs' diameter is $a = 1.4$ m and the draft is $T = 1$ m. The distance from the wall to WEC central axis is $d = 6$ m and the non-dimensional distance between two adjacent WECs is $L/a = 4$. The above configuration was recently studied by Loukegeorgaki et al. [8] in the case of finite breakwater length.

Figure 6 depicts the present method results concerning the normalized total forces $F/\rho g A \pi \alpha^2$, exerted on each WEC of the array, as functions of the angular frequency ω, in the range [1 rad/s, 4 rad/s], as calculated by the present model. The results are derived from the present BEM based on two different computational grids with different numbers of elements in order to verify the convergence of the results. In particular, a medium and a fine mesh are used. In the medium mesh, the wetted surface of each cylindrical WEC is approximated by 1044 quadrilateral elements, while in the fine mesh configuration, each WEC is represented by 1584 elements. The surrounding free surface mesh spans 2.5 wavelengths and is redefined for each frequency. The latter boundary part incorporates the absorbing layer, which is activated one wavelength before the edge of the grid. In the medium mesh case, the free surface is discretized by 15 elements per wavelength and the total mesh size varies from 22,000 to 26,000 elements (for higher frequencies). The increase in the number of elements is a consequence of maintaining a minimum of 15 elements per wavelength on the free surface parts surrounding the WECs, and increased grid resolution is used in the near field; see Figures 4 and 5. In the finer mesh case, the free surface is discretized by using 17 elements per wavelength and the total mesh size varies from 32,500 to 38,600 elements. As observed in Figure 6, the medium mesh provides convergent results for all frequencies.

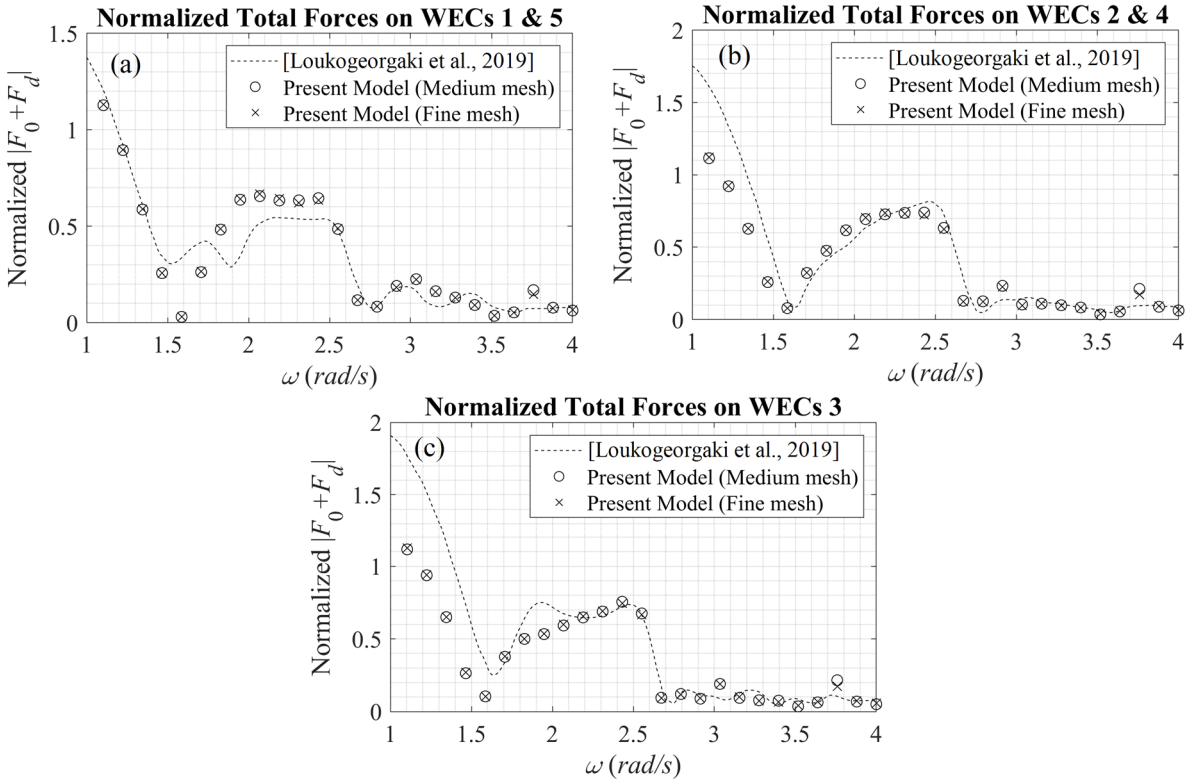

Figure 6. Normalized total vertical forces ($F/\rho g A \pi \alpha^2$) on each WEC of a 5-WEC array; $h = 10$ m, $d = 6$ m, $L/a = 4$ and $\beta = 90°$ [8].

Moreover, in Figure 6, comparisons of the present BEM predictions with the results of Ref. [8] are shown by using dashed lines. As remarked above, in the latter work, the breakwater wall length is finite and equal to $l_W/a = 18$, and thus, the WEC array extends over the whole breakwater. On the contrary, in the present model, the far-field radiation condition is implemented by using an absorbing layer technique, and the results practically correspond to infinite breakwater wall length. The above remark justifies the differences observed between the two data sets. For angular frequencies lower than 1 rad/s, due to the substantial increase in the wavelength, the consideration of the finite breakwater wall configuration of Ref. [8] results in reduced reflection effects as compared to the present method, which is responsible for the differences concerning the excitation forces, and therefore, also the responses, especially in the low frequency band. On the other hand, the infinite wall assumption of the present model results in full-wall reflection of the incident wave for all wavelengths, and the WEC responses that will be examined in more detail in the next section, especially for very low frequencies, are affected by the stationary field generated by the combination of the incident and reflected wave components.

4. Numerical Results

Numerical results are presented in this section for the case of an array consisting of five cylindrical WECs installed in an area of water depth h with $\alpha/h = 0.225$, $T/h = 0.3$, $\frac{d}{a} = 3$, and $L/a = 6$. In the absence of data concerning values of η_{eff}, numerical results for $\eta_{eff} = 1$ are obtained and presented. Moreover, representative values for $B_{PTO} = j\ B_{33,av}$ are used, where $B_{33,av}$ denotes a characteristic value obtained as the frequency average of the calculated hydrodynamic damping coefficient B_{33}, corresponding to the middle (third) WEC of the array, and j is a multiplying factor, defined as $j = [2, 5, 10]$. The PTO stiffness is taken to be $C_{PTO} = [0.1,\ 0.2]\ c_{33}$, corresponding to magnitudes used in the literature; see e.g., [20]. The case $B_{PTO} = C_{PTO} = 0$ is additionally considered, corresponding to an array consisting of freely floating bodies.

The Froude–Krylov (FK) vertical forces acting on the WECs, normalized with respect to ($\rho g \pi A \alpha^2$), are depicted in Figure 7, as functions of the non-dimensional frequency $\omega\sqrt{\alpha/g}$, showing a strong dependence on the direction of propagation of the incident field. In particular, Figure 7 shows the FK forces resulting from propagation at incident wave directions 30°, 60°, and 90°, with the 90° case corresponding to normal incidence on the wall. The case $\beta = 0°$, corresponding to incident wave propagation parallel to the breakwater, is also included. The position of each device only affects the phase of the FK forces, except for the $\beta = 90°$ case, where these forces on all WECs share the same phase. It is observed in Figure 7 that in the low-frequency limit and β different than zero, the normalized FK forces tend to 2, which is due to wall reflection effects on the wave field, since all WECs are placed on an antinode. On the contrary, for $\beta = 0°$ the wall reflection is zero and has no effect. However, the latter case is not expected in practice, since for breakwaters in nearshore/coastal regions, the bathymetry-induced refraction and shoaling effects on the wave propagation will result in incident waves with a direction component towards the wall.

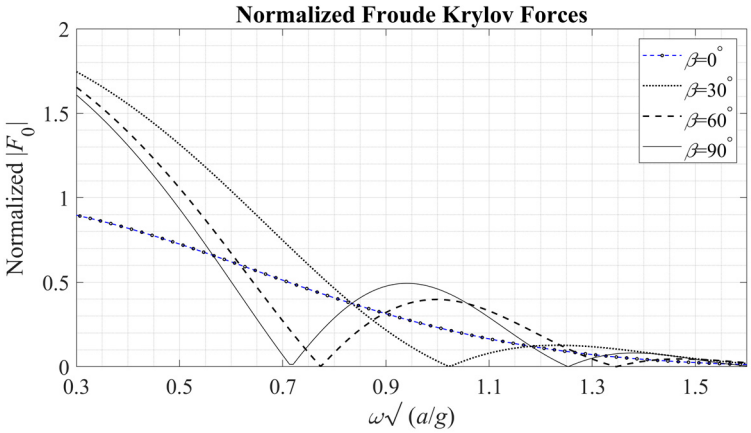

Figure 7. Normalized vertical Froude–Krylov forces on each cylindrical WEC, for incident wave directions $\beta = [0°, 30°, 60°, 90°]$. The geometrical parameters of the WECs and configuration are: $\frac{a}{h} = 0.225$, $\frac{T}{h} = 0.3$, $\frac{d}{a} = 3$, and $L/a = 6$.

Moreover, the diffraction forces on each WEC are shown in Figure 8, and it is observed that they present a complicated pattern as a result of the wall's presence. Furthermore, the diffraction forces on the WECs 1 and 5, as well as on the WECs 2 and 4, are equal in the case of normal incidence to the wall ($\beta = 90°$) due to symmetry of the arrangement and the resulting fields. It is noted that the diffraction forces are different for each WEC in the arrangement, as opposed to the FK forces.

Data concerning the diagonal components of the added mass and the hydrodynamic damping matrices are presented in Figure 9. In particular, Figure 9a shows the diagonal elements of the added mass matrix **A** (normalized with respect to the mass of each WEC: $M = \rho\pi\alpha^2 T$) and Figure 9b shows the (non-dimensional) diagonal elements of the hydrodynamic damping matrix **B** as functions of the non-dimensional frequency $\omega\sqrt{\alpha/g}$. For comparison, non-diagonal elements of the **A** and **B** matrices, corresponding to the middle (third) WEC of the array are presented in Figure 10.

The response amplitude operators (RAOs) of each WEC are shown in Figure 11 for $\beta = [0°, 30°, 60°, 90°]$, as functions of the non-dimensional frequency $\omega\sqrt{\alpha/g}$ for the case of freely floating bodies ($B_{PTO} = C_{PTO} = 0$). In this case, it is observed in Figure 11 that the responses become significant for frequencies near the resonance, especially for $\beta = 90°$, as illustrated in subplot (**e**) of Figure 11, which shows a zoom-in of the response of the central WEC in the band of frequencies near resonance.

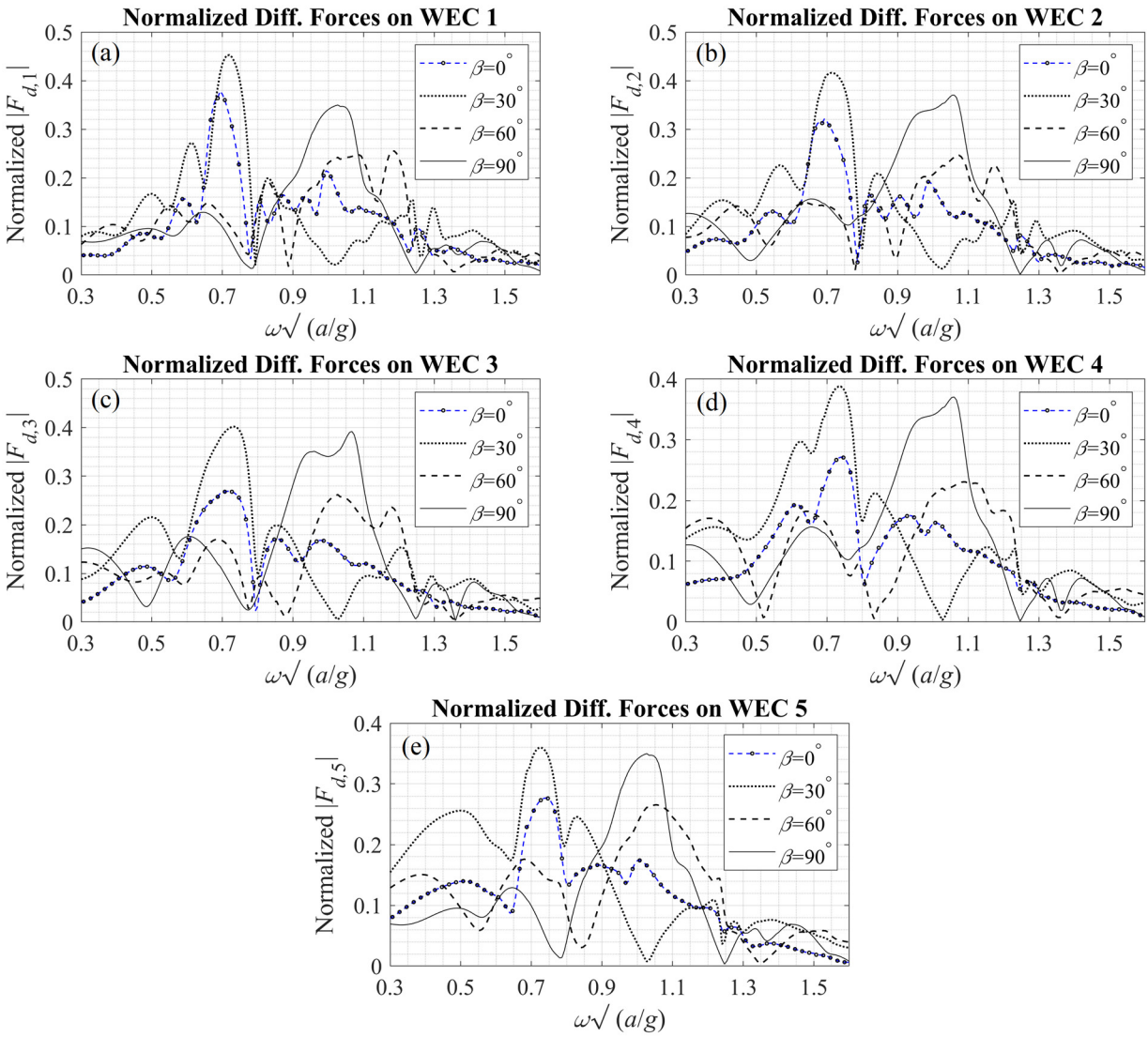

Figure 8. Normalized vertical diffraction forces on each cylindrical WEC, for incident wave directions $\beta = [0°, 30°, 60°, 90°]$. The geometrical parameters of the WECs and configuration are: $\frac{a}{h} = 0.225$, $\frac{T}{h} = 0.3$, $\frac{d}{a} = 3$, and $L/a = 6$.

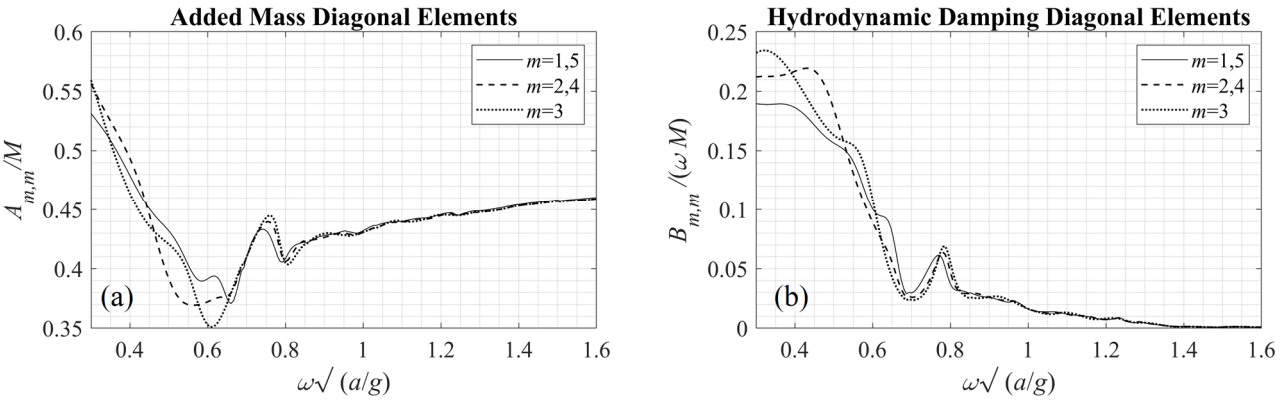

Figure 9. Diagonal elements of the added mass and the hydrodynamic damping matrices, as functions of the non-dimensional frequency, for $\frac{a}{h} = 0.225$, $\frac{T}{h} = 0.3$, $\frac{d}{a} = 3$, and $L/a = 6$.

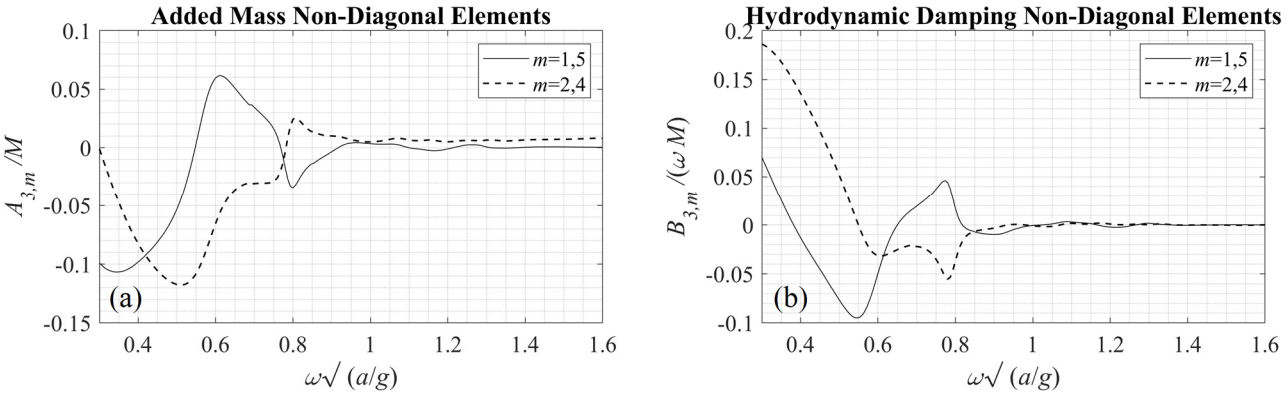

Figure 10. Non-diagonal elements of the added mass and the hydrodynamic damping matrices, as functions of the non-dimensional frequency, corresponding to the middle WEC (third) of the array, for $\frac{\alpha}{h} = 0.225$, $\frac{T}{h} = 0.3$, $\frac{d}{a} = 3$, and $L/a = 6$.

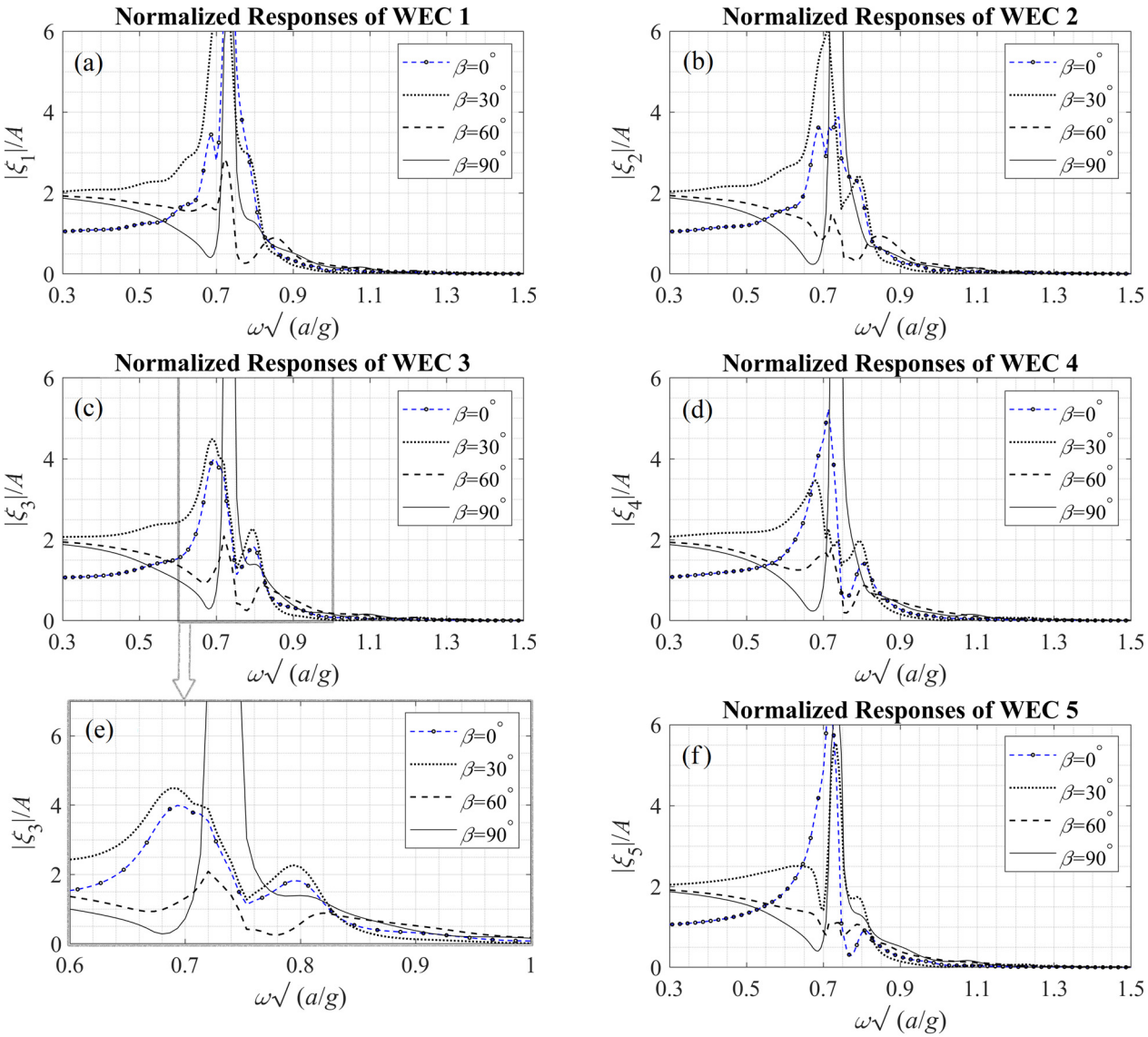

Figure 11. Normalized responses of each cylindrical WEC, for $\frac{\alpha}{h} = 0.225$, $\frac{T}{h} = 0.3$, $\frac{d}{a} = 3$, $\frac{L}{a} = 6$, and $\beta = [0°, 30°, 60°, 90°]$. Subplot (**e**) is a zoom-in of the response of the central WEC (third) in the band of frequencies near resonance.

It is worth noting that the responses of the WECs are highly dependent on the gap between the devices and the vertical wall. Especially in the case of normal incidence, the formation of standing waves leads to low responses when the WECs are centered on a node of the incident field, which corresponds to wavelengths of λ such that $(2n+1)\lambda/4 = d$, $n = 0, 1, 2\ldots$, where d is the distance from the WEC waterplanes' midpoints to the breakwater; see Figure 2. For the considered case, this happens for wavelengths corresponding to non-dimensional frequencies $\omega\sqrt{a/g} = [0.716, 1.25, 1.61, \ldots]$ and the RAOs present a pattern similar to that of the FK forces, which vanish at these points, as shown in Figure 7.

The effect of the PTO parameters on the devices' responses is illustrated in Figure 12 for $\beta = 90°$. In particular, Figure 12a–c shows the responses of WECs 1 and 5, Figure 12d–f shows the responses of the WECs 2 and 4, and Figure 12g–i shows the responses of WEC 3 as functions of the non-dimensional frequency. The PTO stiffness (C_{PTO}) is set to 0 c_{33} in the first column of Figure 12, while in the subplots of the second and third columns, it is set to 0.1 c_{33} and 0.2 c_{33}, respectively. The various subplots of Figure 12 illustrate the responses for $B_{PTO} = [0,\ 2,\ 5,\ 10] \times B_{33,\,av}$. The above, for a dimensional configuration with $a = 1.5$ m, respectively, correspond to the following values of the damping coefficient: 0 Ns/m, 2331.37 Ns/m, 5828.42 Ns/m, and 11,656.85 Ns/m, respectively.

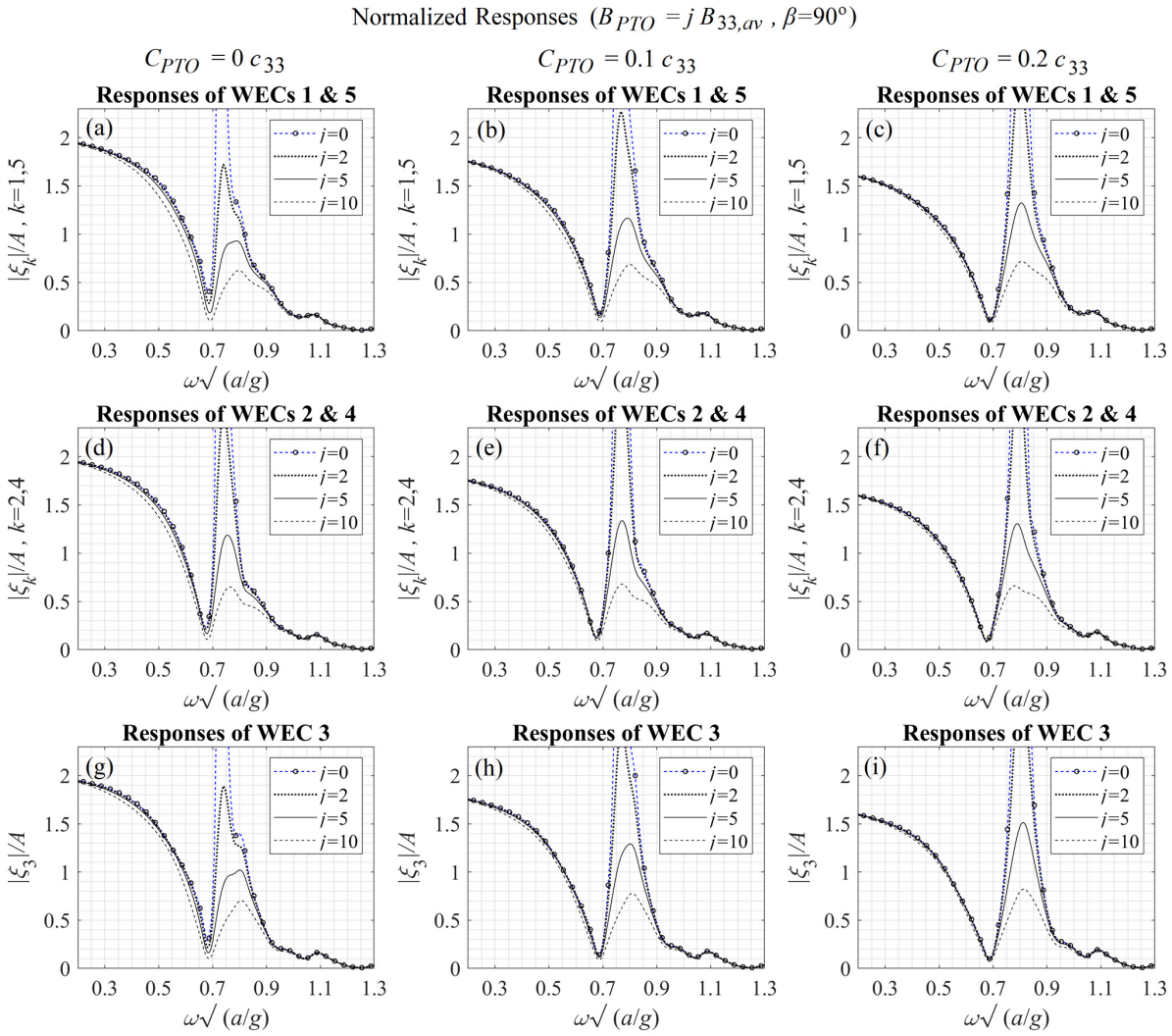

Figure 12. Normalized responses of each cylindrical WEC, for normally incident waves ($\beta = 90°$), in the case of PTO parameters $B_{PTO} = [0,\ 2,\ 5,\ 10] \times B_{33,\,av}$, and (**a**,**d**,**g**) $C_{PTO} = 0 \times c_{33}$, (**b**,**e**,**h**) $C_{PTO} = 0.1 \times c_{33}$ and (**c**,**f**,**i**) $C_{PTO} = 0.2 \times c_{33}$. (**a–c**) Responses of WECs 1 and 5, (**d–f**) Responses of WECs 2 and 4, (**g–i**) Responses of WEC 3.

The resulting performance index (normalized power output) for each WEC of the array, as evaluated by Equation (14), is illustrated in Figure 13. Specifically, $C_{PTO} = 0\ c_{33}$ is shown in the first-row subplots (a, d, g), $C_{PTO} = 0.1\ c_{33}$ in the second-row subplots (b, e, h), and $C_{PTO} = 0.2\ c_{33}$ in the third-row subplots (c, f, i). As expected, higher values of PTO damping lead to decreased peak values of heave response. However, at the same time, they lead to increased power absorption at low frequencies, as shown in Figure 13, since the power output of the WECs' is directly related to the PTO damping, while the RAOs at frequencies below resonance are not gravely affected. As regards the PTO stiffness, it can be seen in Figure 12 that higher values of C_{PTO}, slightly shift the natural frequency and tend to keep the responses lower at the low frequencies range.

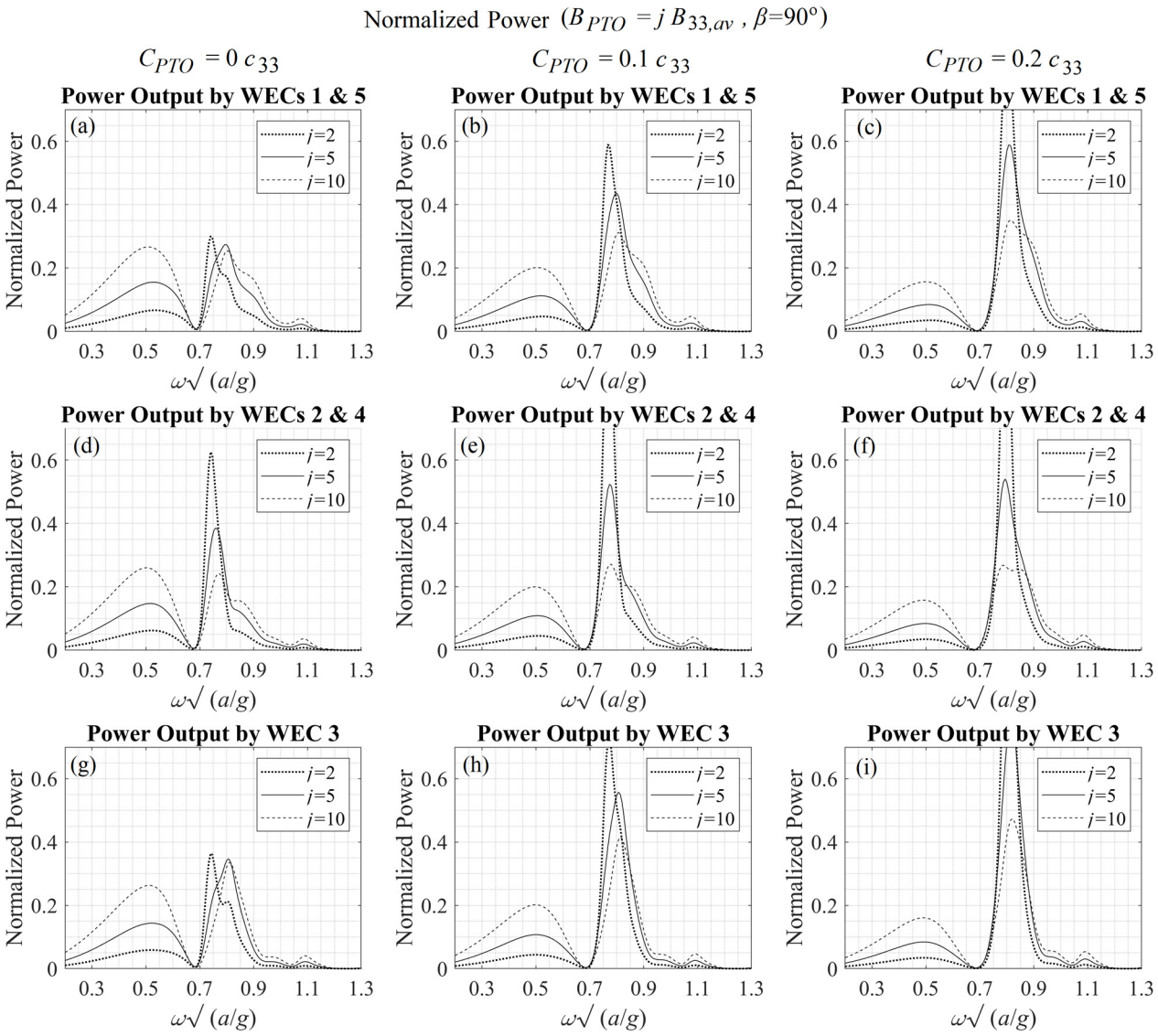

Figure 13. Normalized power output of each cylindrical WEC, for normally incident waves ($\beta = 90°$), in the case of PTO parameters $B_{PTO} = [0,\ 2,\ 5,\ 10] \times B_{33,\,av}$, and (**a**,**d**,**g**) $C_{PTO} = 0 \times c_{33}$, (**b**,**e**,**h**) $C_{PTO} = 0.1 \times c_{33}$ and (**c**,**f**,**i**) $C_{PTO} = 0.2 \times c_{33}$. (**a**–**c**) Power Output by WECs 1 and 5, (**d**–**f**) Power Output by WECs 2 and 4, (**g**–**i**) Power Output by WEC 3.

The present analysis concerns the ideal flow case and serves as a first approximation for the estimation of the system performance. Effects of viscosity on the responses, as well as on the gap resonances could be approximated by introducing additional damping and this is left to be examined in future extensions of the present model.

5. Case Study

The nearshore area at the port of Heraklion, situated in the north coast of Crete Island, in the Southern Aegean Sea, is studied as an example of the application of the considered system in the Greek seas region; see Figure 14. The above nearshore area is characterized by relatively increased wave potential [21] and is thus considered to demonstrate the applicability of the present method, as regards the evaluation of the WEC array's power output.

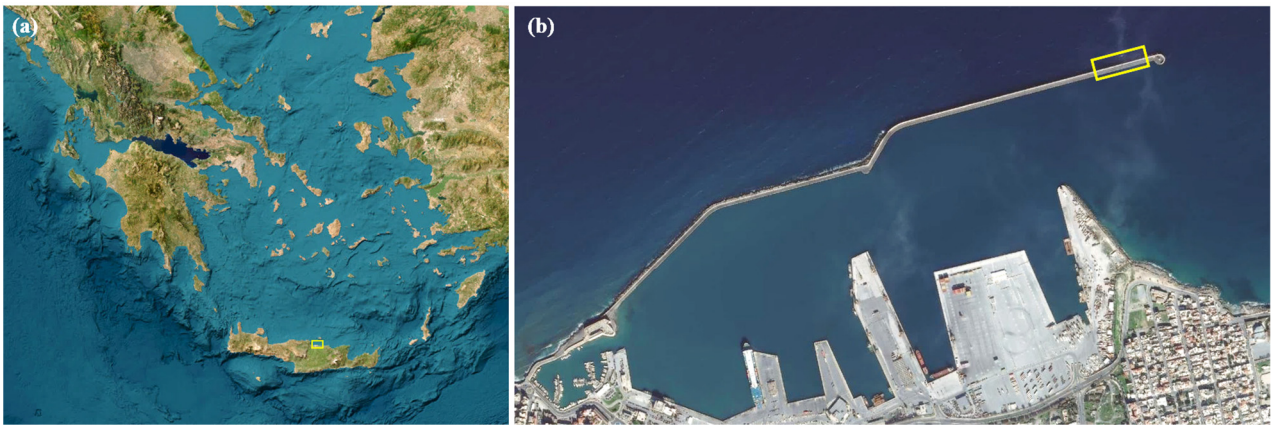

Figure 14. (**a**) Map of the Southern Aegean Sea and the coastal port area of Heraklion in Crete Island shown using the yellow box. (**b**) Port of Heraklion and protective breakwater. The site of the WEC arrangement is indicated by the yellow box.

The wave climatology in the studied area is based on a long-term time series, covering the 10-year period between January 2013 and December 2022, at the offshore points with geographical coordinates 35°30′00″ N–25°00′00″ E and 35°30′00″ N–25°30′00″ E, as derived from the ERA5 database [22]. The relevant information includes significant wave height (H_S), mean energy wave period (T_{-10}), and mean wave direction (θ_m—measured clockwise from the North) with a 3 h temporal resolution. Based on the above data, the offshore wave climatology is derived and presented in Figure 15, where standard lognormal and kernel density univariate and bivariate models are used to represent the distributions. An offshore-to-nearshore (OtN) transformation technique is used to generate nearshore wave data at the target point located at a distance in front of the breakwater with geographical coordinates 35°21′15″ N–25°09′00″ E, as shown in Figure 16. Calculations are based on the SWAN nearshore wave spectral model [23].

Offshore wave conditions, represented by appropriate spectral parameters (significant wave height, mean wave period, and mean wave direction), are considered known all along the seaward boundary from which directional spectrum $S(f, \theta)$ is reconstructed using the JONSWAP frequency spectrum, in conjunction with a hyperbolic cosine spreading function. For the present study, the bathymetric data used are obtained from the General Bathymetric Chart of the Oceans (GEBCO) [24]. The database used for the coastline is the Global, Self-consistent, Hierarchical, High-resolution Shoreline Database (GMT—GSHHS), provided under GNU Lesser General Public License; see [25]. The main forcing of the examined system is represented by the offshore wave conditions, which are continuously distributed along the seaward boundary. Given the offshore boundary conditions, the phase-averaged model SWAN is applied to calculate the wave conditions inside the computational domain with sufficient spatial resolution, as shown in Figure 16. The basic equation used in SWAN model is the radiative transfer equation expressing action balance:

$$\frac{\partial}{\partial t}N + \frac{\partial}{\partial x}c_x N + \frac{\partial}{\partial y}c_y N + \frac{\partial}{\partial \omega}c_\omega N + \frac{\partial}{\partial \theta}c_\theta N = \frac{F}{\omega} \quad (15)$$

where $N = N(\omega, \theta; x, y, t) = S(\omega, \theta; x, y, t)/\omega$ denotes the wave action density, expressed as a function of spectral density S and wave frequency ω. Furthermore, c_x, c_y , c_ω, and c_θ denote propagation velocity components in the physical and the Fourier parameter space, respectively, and F models the forcing source terms, including the effects of wind-generated wave energy, dissipation due to deep-water wave breaking, wave–seabed interactions, and depth-induced wave breaking in shallow water. More details concerning the implementation of OtN wave transformation can be found in Ref. [26].

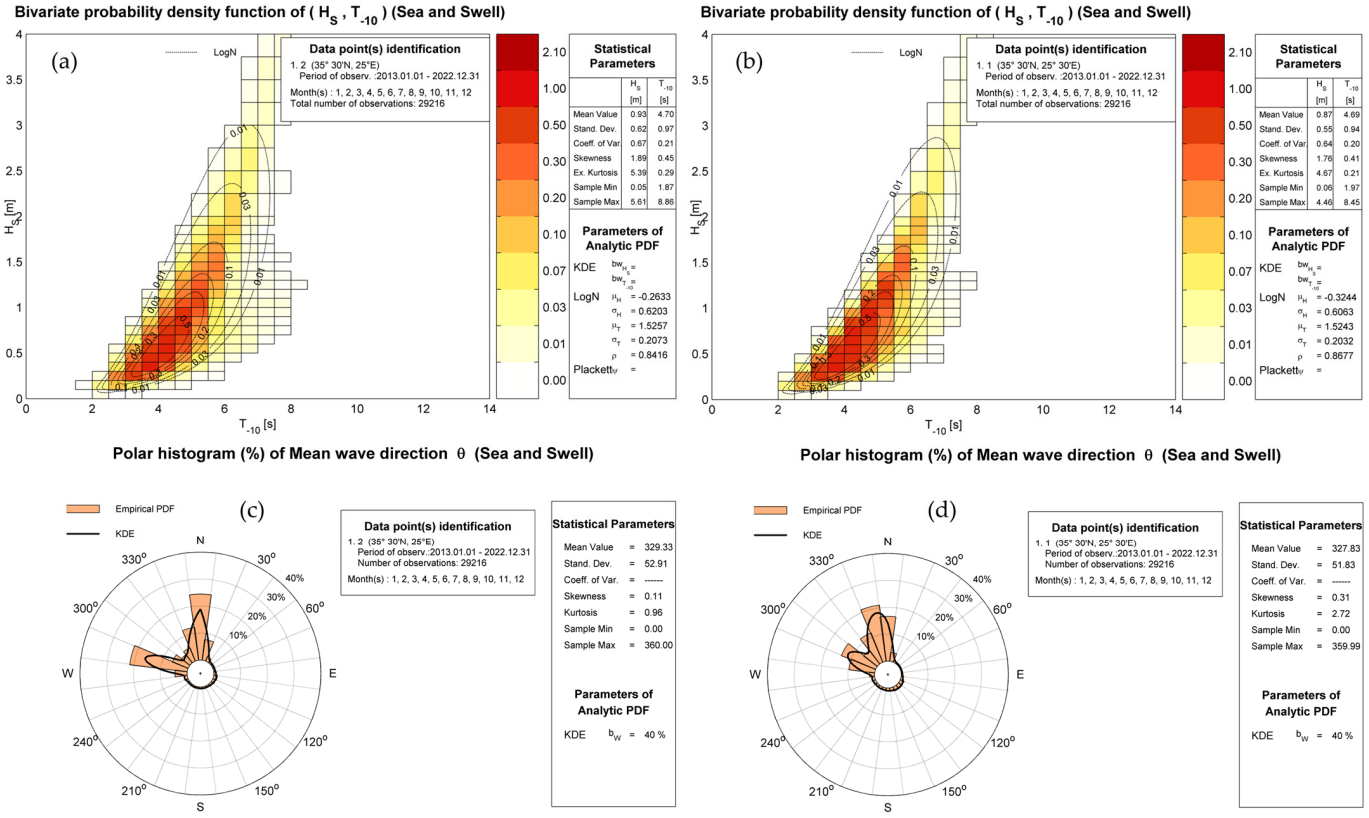

Figure 15. Wave climate data at the offshore points with geographical coordinates (**a**,**c**) 35°30′00″ N–25°00′00″ E and (**b**,**d**) 35°30′00″ N–25°30′00″ E. The bivariate H_S—T_{-10} statistics are presented in subplots (**a**,**b**), and the corresponding wave roses in subplots (**c**,**d**).

Selected results are presented in Figure 17 concerning the spatial distributions of the calculated significant wave height in the domain corresponding to characteristic wave conditions at the offshore boundary. It is clearly seen in this figure that the transformation of wave conditions includes refraction–diffraction and shoaling effects, as well as the sheltering effects by the small island (Dia) at the northern side of the domain. The derived nearshore wave climatology, at the target point located at a distance about 3.5 km from the port of Heraklion breakwater and water depth h = 15 m, as obtained by the present OtN transformation, is presented in Figure 18, and the corresponding basic statistics of the nearshore wave parameters are listed in Table 1.

Table 1. Basic statistics of the wave parameters at offshore and nearshore target points.

Point	H_S (m)	T_{-10} (s)	θ_{peak1} (deg)	θ_{peak2} (deg)
Offshore	0.93	4.70	285	360
Target point	0.67	4.38	315	345

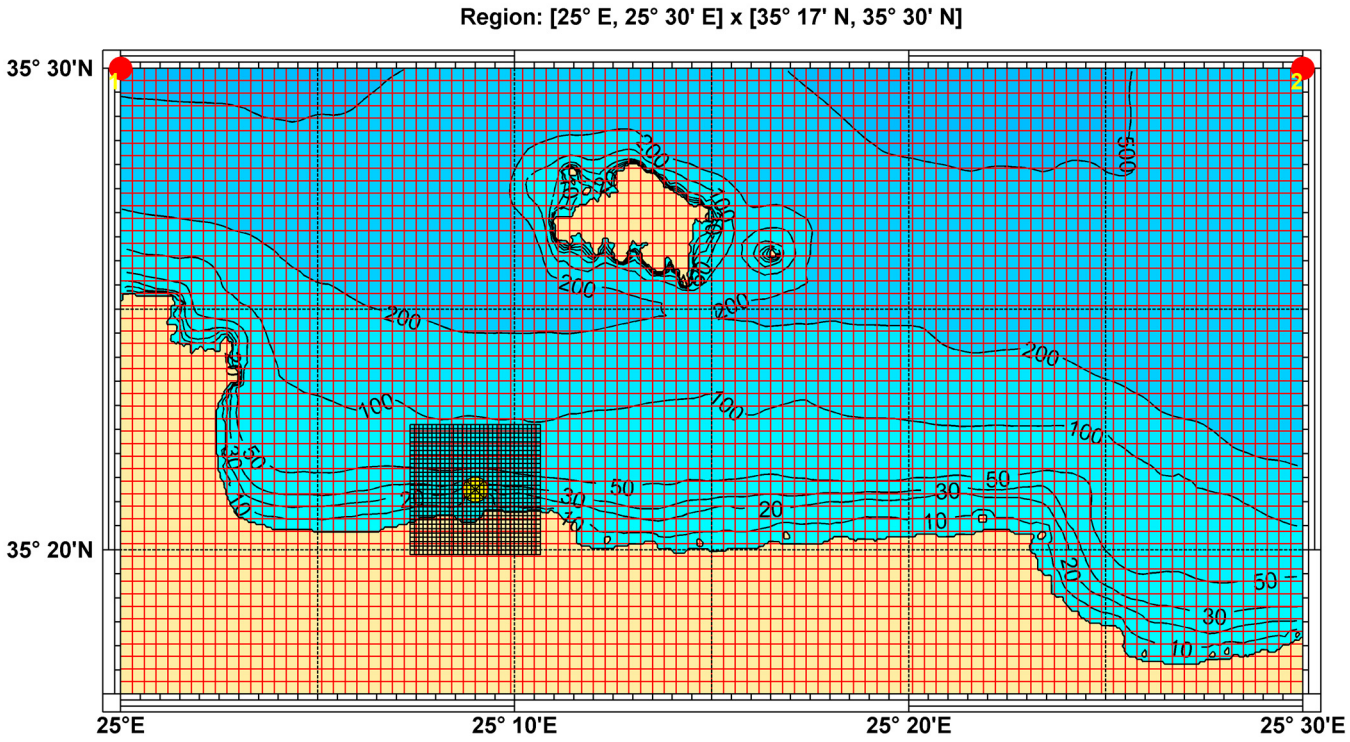

Figure 16. Numerical mesh for the application of the SWAN model, applied to derive the nearshore climatology at the target point in front of the Heraklion port breakwater shown by using a yellow circle. Offshore points are shown by using red circles.

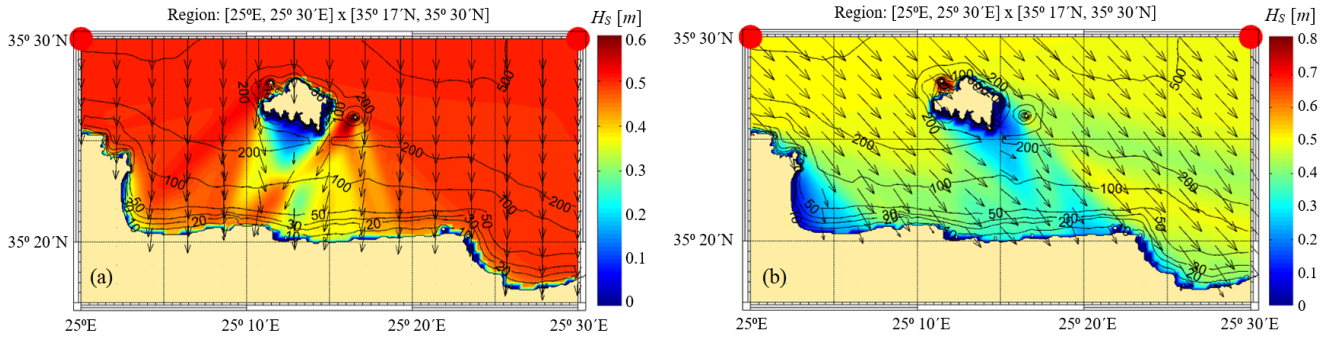

Figure 17. Calculated results of the OtN wave transformation technique using SWAN in the nearshore coastal site of Heraklion in the northern-central part of Crete Island, corresponding to characteristic wave conditions at the offshore boundary from the climatology shown in Figure 15. Incident waves from (**a**) North, (**b**) North-West directions.

In order to quantify the examined WEC array's power output, we consider the five cylindrical WEC arrangements in Heraklion port breakwater where the local depth is equal to $h = 6.67$ m. The floater radius is $a = 1.5$ m and a PTO system is considered with $B_{PTO} = 10B_{33,av}$, which corresponds to $B_{PTO} = 11,650$ Ns/m, and $C_{PTO} = 0.1c_{33}$. Considering all incident wave energy concentrated in the normal direction of the breakwater, the 10-year-long time series of nearshore wave parameters is used to reconstruct wave spectra using the TMA model [27]:

$$S_{TMA}(\omega; H_S, T_{-10}) = S_{JON}(\omega; H_S, T_{-10}) f(\omega; h) \quad (16)$$

where $S_{JON}(\omega\,; H_S,\ T_{-10})$ denotes the JONSWAP spectrum and $f(\omega;\ h)$ the TMA filter function; see also [7]. Each reconstructed spectrum in the time series is discretized into a large number of frequencies $\{\omega_i = i\Delta\omega,\ i = 1, 2, 3 \dots\}$, where $\Delta\omega$ denotes the correspond-

ing constant spacing, and the output power time series of the 5-WEC system is estimated as follows:

$$P = \sum_{k=1,5} \sum_{i} \rho g a \, C_g(\omega_i) A^2(\omega_i) P_k(\omega_i; B_{PTO}) \quad (17)$$

where $A^2(\omega_i) = 2S(\omega_i)\Delta\omega$ and $P_k(\omega_i;\ B_{PTO})$ denotes the normalized power output of the k-WEC, at frequency ω_i and the given B_{PTO}, C_{PTO}, that is estimated using data from Figure 13.

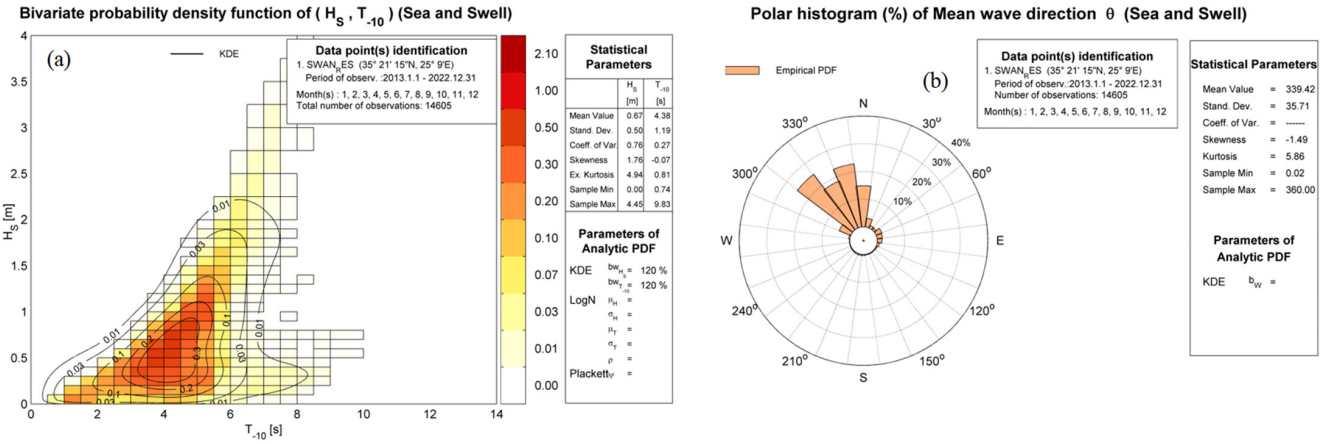

Figure 18. Nearshore wave data at the target point located at a distance 3.5 km in front of the Heraklion breakwater and depth h = 15 m, as obtained by the present OtN transformation.

In Figure 19, the calculated 10-year-long time series of nearshore wave data and power output, by the considered 5-WEC arrangement at the breakwater of Heraklion port, is shown. The annual and seasonal statistics of power production by the system is presented in Figures 20 and 21, respectively, including data concerning mean values and important statistical parameters. Based on the above analysis, the mean power output by the system is 2.04 kW, corresponding to an annual energy production of 17.7 MWh, and the power production is ranging from zero to a maximum value of about 25 kW. For comparison, the corresponding output concerning the same system without the breakwater wall effect is estimated to be 2.3% lower. The energy production by the studied configuration could be further improved by optimal design, and the studied system considered together with the benefits from the facilitation of installation and maintenance of the system and the connection to the grid, could be important for the further consideration of these systems contributing to the greening of energy in ports and harbors.

Regarding practical applications of the considered energy stations, it is evident that the selected devices' natural period in heave can be selected or tuned to coincide with the wave period carrying the highest amounts of energy based on local wave climatology in order to maximize the power production. Further improvement of power output can be achieved by systematic application of the developed BEM model to optimize geometrical, inertial and PTO parameters, and will be the subject of future works. Moreover, in order to reduce the computational cost, the BEM model could be used to derive reduced order models, as the one presented in Ref. [6], which could substantially support the design of the system, by the fast scanning of the multidimensional parameter space, identifying subdomains of best performance. The 3D BEM could be used at the final stage for detailed detection and verification of the optimal solution.

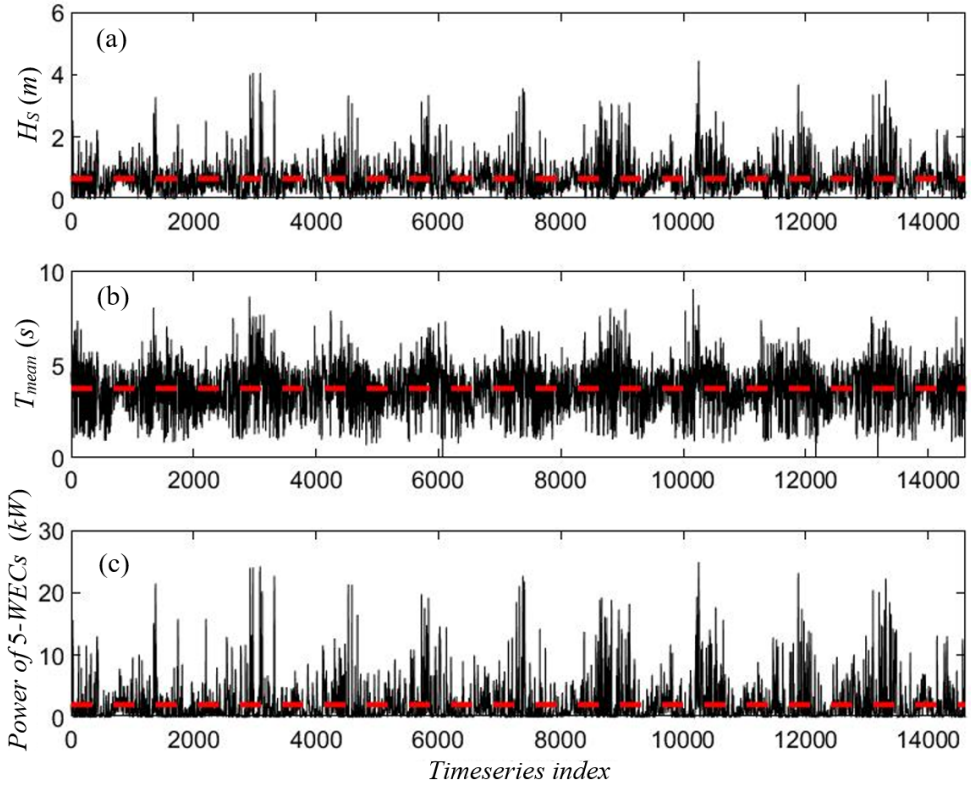

Figure 19. The 10-year-long time series of nearshore wave data and power output by the considered 5-WEC arrangement at the breakwater. (**a**) Significant wave height H_S (m). (**b**) Mean wave period T_m(s). (**c**) Output power by the system (kW). The mean values are indicated by using dashed lines.

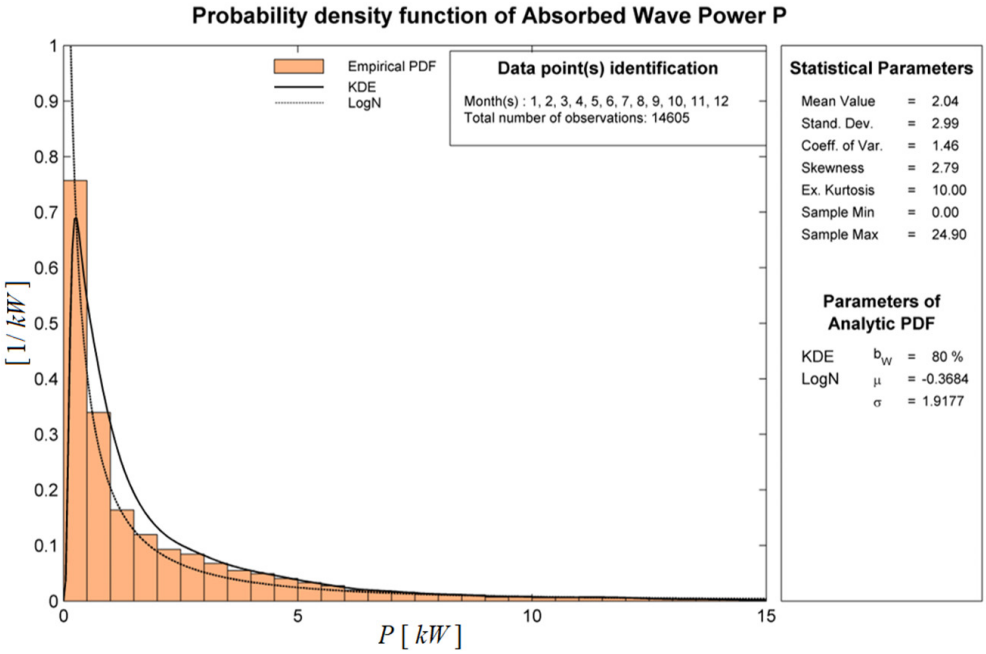

Figure 20. Annual statistics of the power output by the considered 5-WEC system at Heraklion port breakwater.

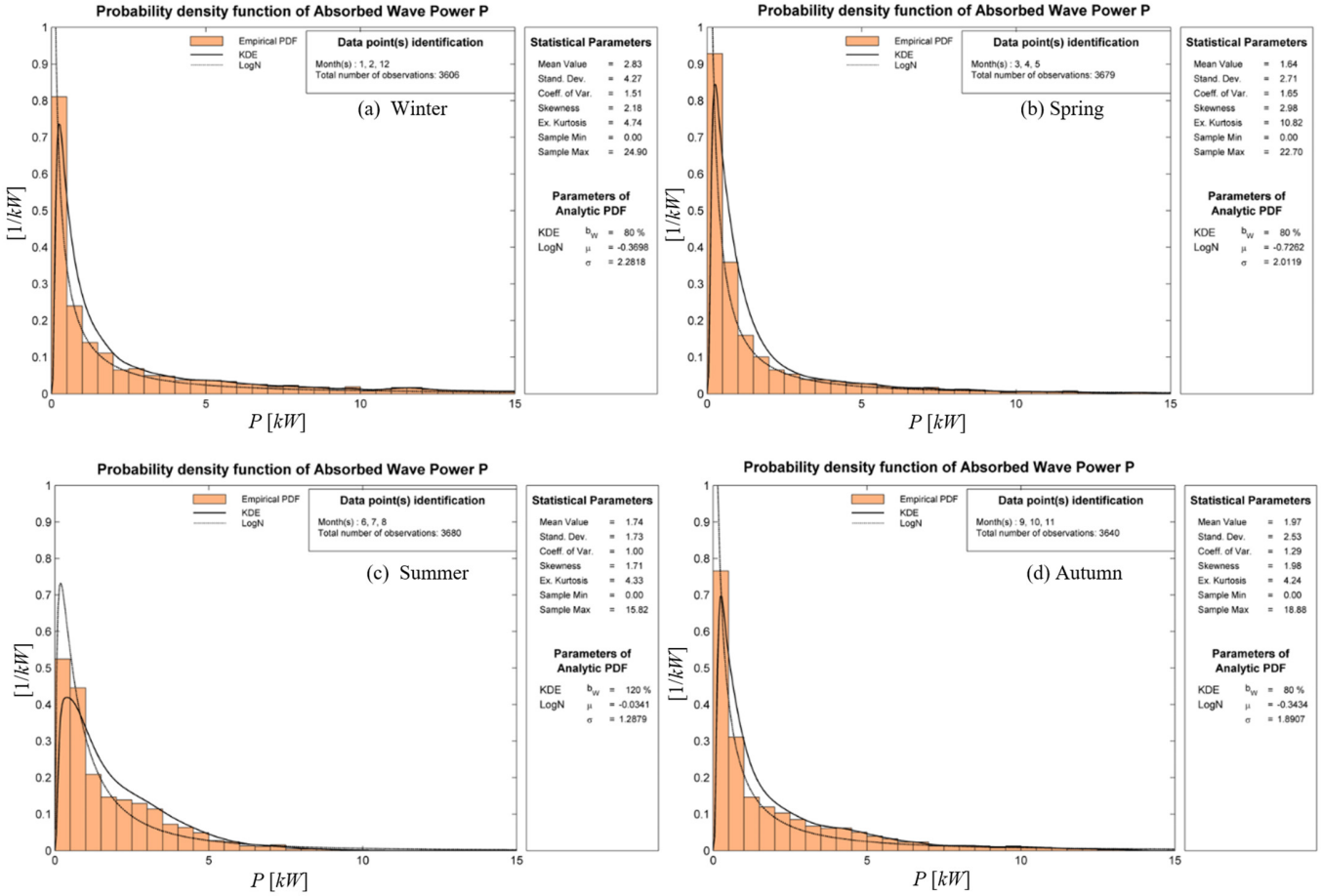

Figure 21. Seasonal statistics of the power output by the considered 5-WEC system at Heraklion port breakwater.

6. Conclusions

In this work, a 3D hydrodynamic model based on the boundary element method (BEM) is presented and discussed, aiming to evaluate the performance of WEC arrays consisting of multiple heaving bodies attached to the exposed side of a breakwater, modelled as a vertical wall. The model accounts for the reflective effects by the wall as well as the hydrodynamic interactions among the multiple devices. Numerical results are presented, accounting for effects of various parameters on power performance, including interactions of multiple floaters, the breakwater wall, as well as the power take off (PTO) system parameters. Finally, a case study is presented based on data of the above numerical model in conjunction with wave climate data at the port of Heraklion, situated in the north coast of Crete Island, in the Southern Aegean Sea, obtained by an offshore-to-nearshore transformation technique. Although the present ideal flow model does not consider the influence of viscosity, which could become significant at specific frequencies associated with gap resonances, it still provides useful results in an extended frequency band and could be exploited for the preliminary evaluation of the system performance and the optimal design and construction contributing to the decarbonization of energy in harbors and neighbor coastal sites. Furthermore, the present BEM method can be easily applied to investigate more general shapes of axisymmetric floaters in one or more degrees of freedom, as well as to study the effects of various control strategies, such as latching techniques that are frequently applied to maximize the power output of the device, by constraining some of the operational characteristics.

Author Contributions: This work was supervised by K.B. The BEM numerical scheme was developed by A.M. and M.B., and the OtN scheme by T.G. The draft of the text was prepared by all authors and the numerical simulations were handled by A.M. and T.G. All authors have read and agreed to the published version of the manuscript.

Funding: This research received no external funding.

Institutional Review Board Statement: Not applicable.

Informed Consent Statement: Not applicable.

Data Availability Statement: Not applicable.

Acknowledgments: A. Magkouris' doctoral studies have been supported by the Special Account for Research Funding (E.L.K.E.) of the National Technical University of Athens (NTUA).

Conflicts of Interest: The authors declare no conflict of interest.

References

1. Babarit, A. *Ocean Wave Energy Conversion*, 1st ed.; ISTE Press-Elsevier: Amsterdam, The Netherlands, 2017.
2. Belibassakis, K.A.; Bonovas, M.; Rusu, E. A Novel Method for Estimating Wave Energy Converter Performance in Variable Bathymetry Regions and Applications. *Energies* **2018**, *11*, 2092. [CrossRef]
3. Stratigaki, V.; Troch, P.; Stallard, T.; Forehand, D.; Kofoed, J.P.; Folley, M.; Benoit, M.; Babarit, A.; Kirkegaard, J. Wave Basin Experiments with Large Wave Energy Converter Arrays to Study Interactions between the Converters and Effects on Other Users in the Sea and the Coastal Area. *Energies* **2014**, *7*, 701–734. [CrossRef]
4. Charrayre, F.; Peyrard, C.; Benoit, M.; Babarit, A. A coupled methodology for wave body interactions at the scale of a farm of wave energy converters including irregular bathymetry. In Proceedings of the 33rd Intern Conference on Offshore Mechanics and Arctic Engineering (OMAE2014), San Francisco, CA, USA, 8 June 2014.
5. McCallum, P.; Venugopal, V.; Forehand, D.; Sykes, R. On the performance of an array of floating energy converters for different water depths. In Proceedings of the 33rd Intern Conference on Offshore and Arctic Engineering (OMAE2014), San Francisco, CA, USA, 8 June 2014.
6. Bonovas, M.; Magkouris, A.; Belibassakis, K. A Modified Mild-Slope Model for the Hydrodynamic Analysis of Arrays of Heaving WECs in Variable Bathymetry Regions. *Fluids* **2022**, *7*, 183. [CrossRef]
7. Loukogeorgaki, E.; Chatjigeorgiou, I. Hydrodynamic performance of an array of truncated cylinders in front of a vertical wall. *Ocean Eng.* **2019**, *189*, 106407. [CrossRef]
8. Loukogeorgaki, E.; Boufidi, I.; Chatjigeorgiou, I.K. Performance of an Array of Oblate Spheroidal Heaving Wave Energy Converters in Front of a Wall. *Water* **2019**, *12*, 188. [CrossRef]
9. Loukogeorgaki, E.; Michailides, C.; Lavidas, G.; Chatjigeorgiou, I.K. Layout optimization of heaving Wave Energy Converters linear arrays in front of a vertical wall. *Renew. Energy* **2021**, *179*, 189–203. [CrossRef]
10. Cheng, Y.; Fu, L.; Dai, S.; Collu, M.; Ji, C.; Yuan, Z.; Incecik, A. Experimental and numerical investigation of WEC-type floating breakwaters: A single-pontoon oscillating buoy and a dual-pontoon oscillating water column. *Coast. Eng.* **2022**, *177*, 104188. [CrossRef]
11. Chen, M.; Xiao, P.; Zhou, H.; Li, C.B.; Zhang, X. Fully Coupled Analysis of an Integrated Floating Wind-Wave Power Generation Platform in Operational Sea-States. *Front. Energy Res.* **2022**, *10*, 931057. [CrossRef]
12. Peng, W.; Zhang, Y.; Yang, X.; Zhang, J.; He, R.; Liu, Y.; Chen, R. Hydrodynamic Performance of a Hybrid System Combining a Fixed Breakwater and a Wave Energy Converter: An Experimental Study. *Energies* **2020**, *13*, 5740. [CrossRef]
13. Gao, J.L.; Zang, J.; Chen, L.; Chen, Q.; Ding, H.; Liu, Y. On hydrodynamic characteristics of gap resonance between two fixed bodies in close proximity. *Ocean Eng.* **2019**, *173*, 28–44.
14. Gao, J.L.; He, Z.; Huang, X.; Liu, Q.; Zang, J.; Wang, G. Effects of free heave motion on wave resonance inside a narrow gap between two boxes under wave actions. *Ocean Eng.* **2021**, *224*, 108753.
15. Gao, J.L.; Lyu, J.; Wang, J.H.; Zhang, J.; Liu, Q.; Zang, J.; Zou, T. Study on Transient Gap Resonance with Consideration of the Motion of Floating Body. *China Ocean. Eng.* **2022**, *36*, 994–1006. [CrossRef]
16. Gao, J.L.; Gong, S.; He, Z.; Shi, H.; Zang, J.; Zou, T.; Bai, X. Study on Wave Loads during Steady-State Gap Resonance with Free Heave Motion of Floating Structure. *J. Mar. Sci. Eng.* **2023**, *11*, 448. [CrossRef]
17. Chen, M.; Ouyang, M.; Guo, H.; Zou, M.; Zhang, C. A Coupled Hydrodynamic–Structural Model for Flexible Interconnected Multiple Floating Bodies. *J. Mar. Sci. Eng.* **2023**, *11*, 813. [CrossRef]
18. Katz, J.; Plotkin, A. *Low Speed Aerodynamics*; McGraw-Hill: San Francisco, CA, USA, 2001.
19. Newman, J. Distributions of sources and normal dipoles over a quadrilateral panel. *J. Eng. Math.* **1986**, *20*, 113–126. [CrossRef]
20. Anderlini, E.; Forehand, D.I.M.; Bannon, E.; Xiao, Q.; Abusara, M. Reactive control of a two-body point absorber using reinforcement learning. *Ocean Eng.* **2018**, *148*, 650–658. [CrossRef]
21. Soukissian, T.; Gizari, N.; Chatzinaki, M. Wave potential of the Greek seas. In *WIT Transactions on Ecology and the Environment*; WIT Press: Billerica, MA, USA, 2011. [CrossRef]

22. Dee, D.P.; Uppala, S.M.; Simmons, A.J.; Berrisford, P.; Poli, P.; Kobayashi, S. The ERA-Interim reanalysis: Configuration and performance of the data assimilation system. *Q. J. R. Meteorol. Soc.* **2011**, *137*, 553–597. [CrossRef]
23. Booij, N.; Ris, R.C.; Holthuijsen, L.H. A third-generation wave model for coastal regions: 1. Model description and validation. *J. Geophys. Res. Ocean.* **1999**, *104*, 7649–7666. [CrossRef]
24. GEBCO Compilation Group. GEBCO 2023. Grid. 2023. Available online: https://www.gebco.net/data_and_products/gridded_bathymetry_data/gebco_2023/ (accessed on 29 July 2023).
25. Wessel, P.; Smith, W.H.F. A global, self-consistent, hierarchical, high-resolution shoreline database. *J. Geogr. Res.* **1996**, *101*, 8741–8743. [CrossRef]
26. Athanassoulis, G.A.; Belibassakis, K.A.; Gerostathis, T.H. The POSEIDON nearshore wave model and its application to the prediction of the wave conditions in the nearshore/coastal region of the Greek Seas. *Glob. Atmos. Ocean Syst.* **2002**, *8*, 201–217. [CrossRef]
27. Massel, S. *Hydrodynamics of Coastal Zones*; Elsevier: Amsterdam, The Netherlands, 1989.